1 # Asperity failure control of stick-slip along brittle faults

2 Ze'ev Reches[1†], Xiaofeng Chen[1,2], and Brett M. Carpenter[1]

3 [1]School of Geosciences, University of Oklahoma, Norman OK 73019

4 [2]Current address: Department of Geology & Geophysics, Texas A&M University, College

5 Station TX 77843

6 [†]Corresponding author, reches@ou.edu

7 **HIGHLIGHTS:**

8 ▪ Stick-slips are spontaneous, unstable events viewed as earthquakes analogues

9 ▪ Stick-slip mechanics are analyzed by the lock-and-fail of asperities on brittle faults

10 ▪ Surface mapping of experimental faults reveals many asperities susceptible to failure

11 ▪ Inherent strength and fault geometry control events' stress-drop and slip-distance

12

ABSTRACT

Stick-slips are spontaneous, unstable slip events during which a natural or man-made system transitions from a strong, sticking stage to a weaker, slipping stage. Stick-slips were proposed by Brace and Byerlee (1966) as the experimental analogue of natural earthquakes. We analyze here the mechanics of stick-slips along brittle faults by conducting laboratory experiments and by modeling the instability mechanics. We performed tens of shear tests along experimental faults made of granite and gabbro that were subjected to normal stresses up to 14.3 MPa and loading velocities of 0.26-617 μm/s. We observed hundreds of spontaneous stick-slips that displayed shear stress drops up to 0.66 MPa and slip-velocities up to 14.1 mm/s. The pre-shear and post-shear fault surface topography were mapped with atomic force microscopy at pixel sizes as low as 0.003 μm^2. We attribute the sticking phase to the locking of touching asperities and the slipping phase to the brittle failure of these asperities, and found that the fault asperities are as strong as the inherent strength of the host rock. Based on the experimental observations and analysis, we derived a mechanical model that predicts the relationships between the measured stick-slip properties (stress-drop, duration, and slip-distance) and asperity strength.

1. INTRODUCTION

Stick-slips are spontaneous, unstable slip events that have been observed in high-pressure rock-mechanics experiments (Brace and Byerlee, 1966) and nanoscale systems (Rastei et al., 2013). It is generally agreed that these events reflect intense and abrupt weakening during which a physical system transitions from a strong, sticking stage to a weaker, slipping stage; yet, the controlling mechanisms are not universal. Stick-slips have been widely observed in laboratory experiments of shear along experimental faults (e.g. Engelder and Scholz, 1976; Leeman et al., 2018). Brace and Byerlee (1966) indicated the similarity between the instability of experimental stick-slips and natural earthquakes, and postulated that they are the laboratory analogues of natural earthquakes. However, Brace and Byerlee (1966) did not analyze the mechanical processes that control the stick-slips, and later Scholz (1992) stated "[…] the crowning achievement […] of W.F. Brace was the announcement, in Brace and Byerlee (1966), of the stick-slip theory of earthquakes. This constituted a new paradigm for a major earth process, with a potential influence that extended far beyond the confines of Brace's field of rock mechanics

2

42 […] this paradigm has not yet, 25 years later, been consensually accepted into the world view of

43 seismologists […]. If the measure of completion of a scientific revolution is the near-universal

44 acceptance of a new paradigm, then this one is certainly not over." The observed weakening was

45 widely explained in terms of the static/dynamic friction formulation (Dieterich, 1978; Scholz,

46 1998), but friction formulation does not reveal the physical processes controlling the weakening.

47 We focus here on the mechanical processes associated with stick-slips along brittle experimental

48 faults.

49   Typically, stick-slips along experimental faults are short-lived events with durations of

50 microseconds to milliseconds, displacements up to a few tens of microns, and slip velocities of a

51 few cm/s to ~ 1 m/s (e.g., Ohnaka et al., 1987). Stick-slip events are typically associated with

52 intense, rapid weakening during which the shear-stress may drop by 10-70% (Brace and Byerlee,

53 1966; Jaeger and Cook, 1969; Karner and Marone, 2000). This intense weakening occurs over

54 very short slip-displacements of a few tens of microns that differs from dynamic weakening in

55 high-velocity rock friction experiments, in which comparable intense weakening occurs only

56 after long displacements of 0.5 - 2 m or even more (e.g., Niemeijer et al., 2011; Di Toro et al.,

57 2011). Therefore, the weakening mechanisms that were documented for high velocity

58 experiments, with long displacements (e.g., Di Toro et al., 2011; Reches and Lockner, 2010;

59 Chen et al., 2017), cannot be activated during the short displacements of stick-slip events. We

60 thus consider here asperity failure as the weakening mechanism of stick-slips.

61   Byerlee (1970) recognized the above difficulties and proposed that "an instability caused by

62 sudden brittle fracture of locked regions on surfaces in contact is the most likely explanation for

63 stick-slip during dry frictional sliding of brittle rocks at room temperature." This conclusion was

64 partly based on the experimental work of Byerlee (1967) which indicated that faults with highly

65 smooth surfaces have friction coefficients $\mu \sim 0.1$, whereas faults with interlocking asperities

66 displayed $\mu \sim 1.3$. Many experiments have demonstrated that slip along bare surfaces of brittle

67 rocks is dominated by the failure of isolated asperities (Fig. 1) (Scholz and Engelder, 1976;

68 Boneh et al., 2014; Tesei et al., 2017; Yamashita et al., 2018; Boneh and Reches, 2018). Further,

69 the concept of asperity failure was adopted as a mechanism of unstable slip and radiation in

70 experimental observations (McLaskey and Glaser. 2011), and seismic radiation of natural

71 earthquakes (Das and Kostrov, 1986). We follow the hypothesis of Byerlee (1970) and analyze

72   the mechanics of stick-slips as events governed by brittle asperity failure. We test the model

73   derivations by shear experiments with granite and gabbro faults and nanoscale observations.
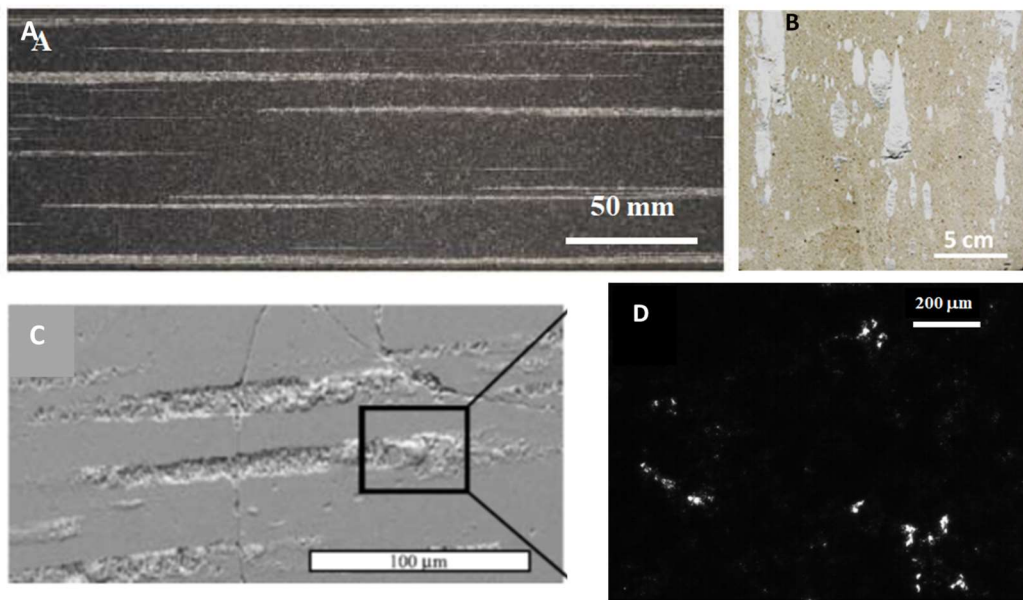
74

75   **Figure 1.** *Close-up of experimental fault slip surfaces displaying fragmented asperities and*

76   *surface damage under shear at the noted normal stress (A-C) and prior to shear (D). A.*

77   *Metagabbro, σ_n = 6.7 MPa (Yamashita et al., 2018); B. Limestone, σ_n = 5 MPa (Tesei et al.,*

78   *2017); C. Granite σ_n = 20 MPa (Koizumi et al., 2004); D. Asperity contacts of a quartz block σ_n*

79   *= 30 MPa before shear (Dieterich and Kilgore, 1996).*

80   **2. MICROMECHANICS OF STICK-SLIPS**

81   2.1 HYPOTHESIS

82   We consider a fault that is composed of two brittle blocks with planar, rough surfaces (Fig. 2).

83   The fault is under normal stress and is loaded by a constant, remote velocity parallel to the

84   surfaces. The blocks contact each other at touching asperities (Fig. 2A), and the real contact area,

85   A_a, is a small fraction of the nominal fault area, A_o, i.e., $r = A_a/A_o \ll 1$. The local stresses at the

86   touching asperities are amplified relative to the macroscopic, nominal applied stress, and the local

87   stress can be as high as the material strength (Tabor, 1975, 2006). On a planar fault with a small

88   r, the touching asperities are isolated (Fig. 1D) (Dieterich and Kilgore, 1996), and are not likely

89   to interact with each other.

90   The considered evolution of a stick-slip event is schematically shown in Figs. 2B-2D. First,

91   the normal stress is supported by a pair of asperities at site #1 that locks the fault. Then, upon

92   remote velocity loading, the shear stress increases locally, deforms the locked asperities, and the

93   upper asperity at site #1 starts climbing over the lower asperity which increases the local normal

94   stress, shear stress, and dilation (small, black arrows at site #1, Fig. 2B). Eventually, the local

95   stresses exceed the asperities' strength, the asperities fail, and the upper block slips with no

96   resistance between the isolated asperities (Fig. 2C). The slip induces simultaneous drop of the

97   normal and shear stresses, and compaction relative to the locked stage. The slip continues until a

98   new pair of asperities come into contact at site #2 (Fig. 2D). If the local stresses at site #2 are

99   below the asperities' strength, the fault enters a new sticking stage (Fig. 2D) of a new stick-slip

100   cycle.

101   This idealized model of the stick-slip process is described for two pairs of asperities.

102   However, in a physical rock experiment, the locking-and-failure stages occurs at assemblages of

103   touching asperities that lock and fail quasi-simultaneously. Finally, the present model considers

104   isolated asperities on a planar, rough fault, without reference to the friction coefficient or the

105   presence of a gouge or a granular layer between the two blocks. The effects of such layers are

106   discussed later.
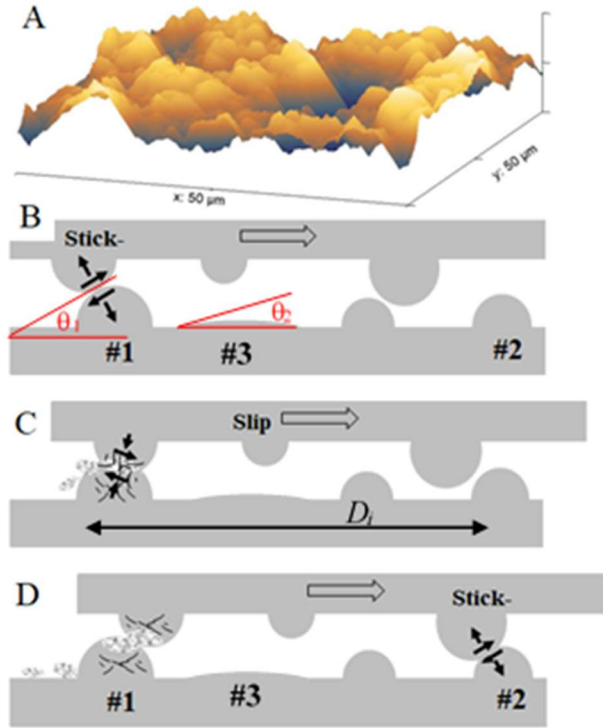
Figure 2. *Stick-slip model configuration. A. Surface topography of a planar, rough surface of a granite block; ground flat and roughened with #600 powder; mapped by AFM (note scales). B-D. Display of the three stages of an idealized stick-slip event (see text).*

2.2 STRENGTH AND FAILURE OF FAULT ASPERITIES

We investigate the mechanics of stick-slips along experimental faults in terms of the above hypothesis: the stick stage is controlled by locked asperity pairs (#1 in Fig. 2), and the slip stage indicates their failure and re-locking by another pair (#2 in Fig. 2). The characteristics of the ith stick-slip event are determined by two parameters: (1) The yielding strength, U_i, of the locking asperities, and (2) The slip-distance, D_i, between the yielding asperities and the next, re-locking asperities (arrow in Fig. 2C). Thus, U_i controls the peak shear-stress, τ_p, of the fault before slip initiation, and D_i controls the slip distance during the event. For shear experiments at room conditions, the yielding strength, U_i, depends on several properties: S, the strength of the fault rocks (the strength will be defined later); R, the shape of the asperities; σ_n, the applied normal stress; and the time for asperity healing and/or creeping during the sticking period. The sticking

123   period depends on the applied remote velocity, V (e.g. Karner and Marone, 2000). Thus, the

124   locking asperity strength is

125    $$U_i = f\ (S, R, \sigma_n, V). \qquad (1)$$

126   The interrelationships of these properties are evaluated below by using the experimental

127   observations. Finally, during the slip stage, part of the accumulated elastic energy is released, and

128   the stress-drop of the ith event is

129    $$\Delta\tau_i = K \cdot D_i \qquad (2)$$

130   where K, and D_i are the elastic stiffness of the loading system and the slip-distance during the

131   event, respectively.

132   2.3 ASPERITY LOAD

133   As shown in equation (1) above, the asperity strength, U_i, is a manifestation of a few

134   mechanical properties, and to resolve their relationships we follow the analyses of Greenwood

135   and Williamson (1966), Whitehouse and Archard (1970), and Tabor (1975). They explored the

136   mechanics of pressing a metal block with rough surface against a flat metal block, a configuration

137   similar to the present idealized model in Fig. 2. The application of normal stress, σ_n, in this

138   setting increases the asperities contact area by the combination of elastic deformation, asperity

139   failure, and bringing additional asperities into contact (Dieterich and Kilgore, 1996; Tabor,

140   2006). Due to these processes, the normal stress at the touching asperities, σ_A, can be roughly

141   considered independent of the nominal, applied normal stress, σ_n (Greenwood and Williamson,

142   1966). Tabor (1975) derived a simple, general expression for the asperity normal stress, σ_A,

143    $$\sigma_A \approx E \tan \theta \qquad (3)$$

144   where θ is the local slope of the asperities (shown schematically in Fig. 2B) and E is the Young's

145   modulus of the blocks (Tabor, 1975, equation 5).

146   Next, these analyses (Greenwood and Williamson, 1966; Whitehouse and Archard, 1970),

147   assumed that plastic deformation initiates at the asperities when the stress exceeds the hardness,

148   H, of the metal. Hardness integrates multiple failure properties including plasticity, and

149   brittleness (Boneh and Reches, 2018), and it is measured at small scales, which are relevant to the

150   asperities' size. The derivations of Tabor (1975) demonstrate that the transition from elastic

151 deformation to plastic deformation occurs at asperities with local slopes which exceed the critical

152 angle θ_C of

153
$$\tan \theta_C = (0.6 \sim 1.0) \frac{H}{E'} \qquad (4)$$

154 where E' is the Young's modulus (for either 2D or 3D). Tabor (2006, Table 7.1) applied equation

155 (4) to several industrial materials and found that the critical slope angle ranges from $\theta_C \sim 0.5°$ for

156 annealed metals to $\theta_C > 20°$ for cross-linked plastics (Table 1). Equation 4 implies that in our

157 model, an asperity with large $\theta_1 > \theta_C$ (#1 in Fig. 2B) is susceptible to failure, whereas an asperity

158 with small $\theta_2 < \theta_C$ (#3 in Fig. 2B) will deform only elastically.

159 2.4 AN EXPERIMENTAL INVESTIGATION OF THE MODEL

160   In the above sections (2.1-2.3), we presented a model of stick-slip mechanics based on

161 asperity failure (Fig. 2). In the following sections, we test this model by describing the observed

162 stick-slips in our experiments with granite and gabbro faults, and then investigating the

163 observations considering the above model. We follow these steps:

164 A. We use atomic force microscopy (AFM) to map the surface topography of planar, rough

165   experimental faults (Appendix). The AFM data is used to determine the local slopes of the

166   mapped surfaces, and the fraction of the surface slopes at angle θ.

167 B. Asperities with local slope equal or exceeding the critical slope, $\theta \geq \theta_C$, (equation 4) are

168   susceptible to fail, and we use the fraction of failure susceptible asperities to evaluate the

169   asperities strength, U_i (equation 1). It is again noted that non-touching asperities (too low),

170   and asperities with $\theta < \theta_C$ are not expected to fail.

171 C. In our model (Figs. 2B-2D) the slip-displacement during a stick-slip event is controlled by the

172   distance between touching asperities that are capable of locking and failing. We measure the

173   distances between the peaks of high asperities on the AFM images, and we expect that the

174   high asperities on one block will be the first to touch the high asperities in the opposite block.

175   Thus, it is assumed that the measured asperity distances are comparable to the slip-

176   displacements during the experimental stick-slips.

177 D. The present analysis focuses on stick-slip mechanics in terms of brittle failure of fault

178   asperities, and the analysis centers on strength parameters (U_i, S, and H in above equations)

179   and fault geometry parameters (R, D_i, and θ in above equations). No attempt is made to

180   investigate the effects of normal stress and applied velocity (equation 1).

181   E. The present experimental setting, similar to common rock friction apparatuses, does not allow

182   for the analysis of a single asperity on a flat surface or two touching asperities. Thus, we

183   examine the asperities on AFM images of one fault block, and assume that the opposite block

184   has similar asperity distribution.

185   **3. EXPERIMENTAL OBSERVATIONS**

186   3.1 EXPERIMENTAL SETTING AND PROCEDURE

187   We conducted shear experiments on a rotary shear apparatus that is described in the Appendix

188   and by Reches and Lockner (2010). The experimental faults were composed of Sierra White

189   granite (SWG) and Raven Noir gabbro (RNG). The samples are cylindrical with a raised ring

190   (Fig. A1A), and the bare fault surfaces were ground flat, followed by roughening with #600

191   powder (Appendix). The ring geometry provides a closed loop fault with a continuous boundary

192   condition (i.e., without an 'end') that is equivalent to an infinitely long fault. During the

193   experiments, the fault was loaded to a constant normal stress ranging from 10.2 to 14.3 MPa and

194   subjected to constant remotely applied velocities ranging from 0.26 to 617 μm/s. The monitoring

195   system continuously record the shear stress, normal stress, and displacement along the fault

196   (Table A1). Note that both shear stress and fault displacement are measured at the base of the

197   blocks that were ~10 cm away from the fault surface (Appendix). Thus, the measured

198   displacement and velocity values were corrected to reflect slip along the fault surface (section

199   4.3). A typical experiment includes an early stage of quasi-linear increase of the shear stress

200   while the fault is locked (Figs. 3A, B) followed by a stage of multiple stick-slip events (insets in

201   Figs. 3A, B) similar to previous experimental observations (e.g., Karner and Marone, 2000).

202   3.2 OBSERVATIONS

203   *3.2.1 Periodic stick-slips*

204   We analyzed 209 stick-slips in 15 runs on the RNG fault under normal stresses of 11.7-14.2

205   MPa and applied velocities of 0.26-9.54 μm/s. The stick-slips display repeatable, systematic

206   periodicity (Fig. 3A) that is controlled by the applied normal stress and remote slip-velocity. The

207   events display stress-drops of 0.05 to 0.6 MPa, event displacements of 3.25 to 17.58 μm, rise-

208   times of 101 to 780 ms, and peak slip-velocities of 28 to 257 μm/s (Table A1). The experiments

209   were conducted in a sequence of 15 runs without treatment of the fault surfaces between the runs

210   and, accordingly, the stick-slip events are divided into three groups based on the experimental

211   sequence. Group RNG1 includes runs after initial roughening, group RNG2 followed group

212   RNG1, and for group RNG3, the normal stress was increased to $\sigma_n = 14.2$. As shown below, the

213   three groups reveal the same systematic characteristics, but vary by the intensity of the events,

214   most likely due to shear modification of the fault surface. For the RNG sample in our loading

215   system, the measured shear stiffness and normal stiffness are 0.184 MPa/μm and 0.171 MPa/μm,

216   respectively.

217   *3.2.2 Non-periodic stick-slips*

218   We analyzed 281 stick-slips in 22 runs on the SWG fault under normal stresses of 10.5-14.3

219   MPa and applied velocities of 16-617 μm/s. Unlike the RNG fault, stick-slips on the SWG fault

220   are non-periodic and irregular in timing, and typically are preceded by a creeping stage (Fig. 3B).

221   These stick-slips have stress-drops ranging from 0.009 to 0.663 MPa, event displacements

222   ranging from 0.09 to 11.92 μm with no clear dependence on normal stress or loading rate over

223   the ranges tested. The duration of these irregular stick-slips ranges from 0.4 to 1.6 ms, resulting

224   in high peak slip-velocities ranging from 188 to 14,159 μm/s (Table A1). The measured shear

225   stiffness of the SWG sample in our loading system is 0.089 MPa/μm, and the measured normal

226   stiffness is 0.092 MPa/μm.

227   The stick-slips along the SWG fault display three stages. First, after the preceding slip event, the

228   shear stress increases linearly, and the fault is loaded elastically (Zone "Elastic" in Fig. 3C).

229   Then, the fault reaches the yielding point (Yield in Fig. 3C), and switches to non-linear creep to

230   peak stress (Peak in Fig. 3C). The fault is no longer locked during the creep stage, and it may

231   accommodate long slip-distance during this stage. Finally, the fault reaches another major slip

232   stage with an abruptly high-velocity slip over a short duration, associated with shear and normal

stress drops and acoustic emission (Fig. 3C). Stick-slips along the SWG fault were observed only

at normal stresses higher than 10 MPa.
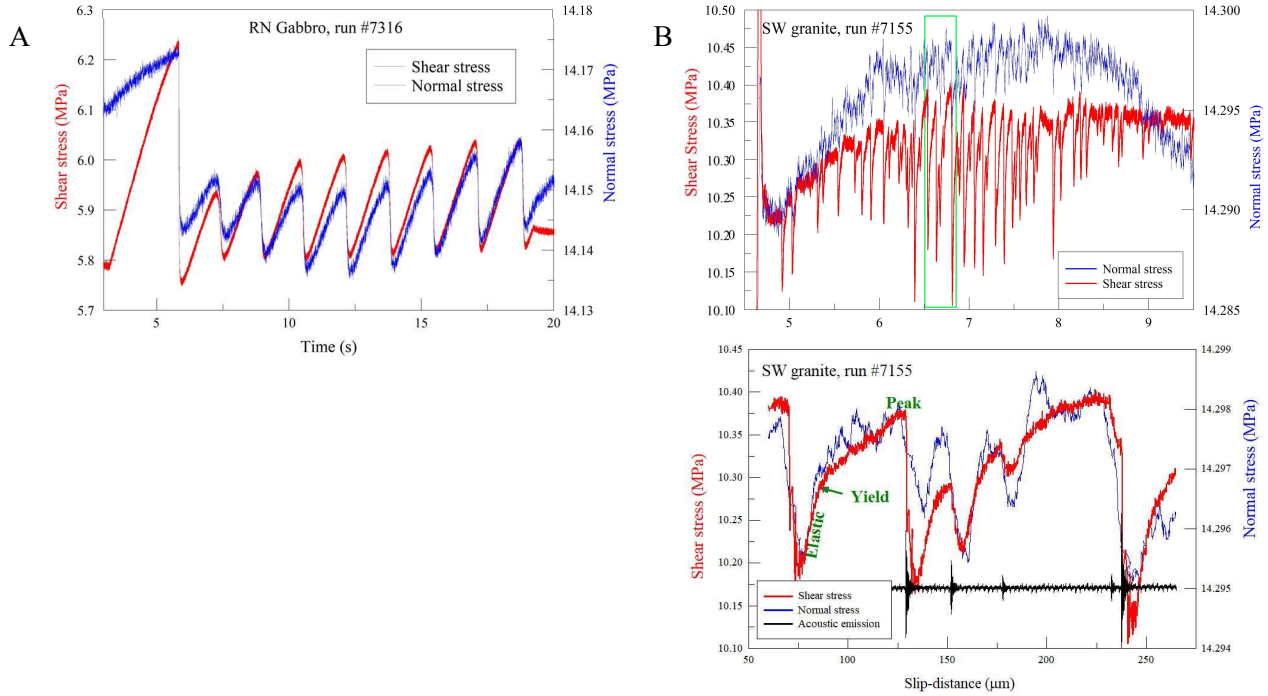
Figure 3. *Experimental observation of stick-slips; note the synchronous rise and drop of the shear and normal stresses in the three plots with separate scales for the two stress components. A. Periodic events along a gabbro fault (run 7316 with applied remote velocity of 3.87 μm/s (Table A1). B. Non-periodic events along a granite fault (run 3155) with remote velocity of 617 μm/s. C. Details of the green rectangle in 3B; 'Elastic', 'Yield' and "Peak' mark phases of the stick stage; acoustic emission acceleration shown at arbitrary scale (see text).*

4. MODEL INVESTIGATION

In the present experiments, we identified and analyzed 490 stick-slip events in 37 shear runs along granite and gabbro faults (above). We now use these data to test the proposed model. The model predicts the relationships between fault geometry and asperity strength U_i (equations 1, 4) and the relations between stress-drop and asperity distribution and loading stiffness (equation 2).

4.1 FAULT ROUGHNESS CONTROL OF ASPERITY BRITTLE FAILURE

The brittle failure of isolated asperities during fault slip has been experimentally observed (Fig. 1), but the geometrical control of this failure has not been quantified for rock faults. Based

11

249   on the analyses of plastic deformation of metal surfaces (Greenwood and Williamson, 1966;

250   Tabor, 1975, 2006), we proposed above that equation (4) can serve as the critical condition for

251   brittle failure of asperities on a planar, rough rock surface. The relevant properties for this

252   condition are Young's modulus (E), hardness (H), and local surface slope (θ). The first two

253   properties are available from published rock-mechanics analyses (Table 1). Boneh and Reches

254   (2018) showed that micro-hardness is an effective variable to quantify the failure of brittle

255   asperities on experimental faults composed of granitic, carbonate, and sandstone blocks (their

256   Fig. 5). Table 1 indicates that for the measured ranges of E and H, the critical asperity slope for

257   brittle failure is in the range of 6° - 17° for granite and gabbro. Namely, asperities with slopes

258   below these critical angles will deform elastically, whereas asperities with larger slopes will fail

259   in a brittle style.

260   To quantify the asperities slopes, we used an AFM to map roughened surfaces of the

261   experimental faults (Appendix). AFM maps cover regions of tens of microns (Chen et al., 2013),

262   which is the relevant scale of slip-displacements for the experimental stick-slips (Table A1). We

263   mapped 6 polished pre-shear surfaces and 13 post-shear surfaces from SWG, and 4 post-shear

264   surfaces from gabbro. As we did not have pre-shear gabbro samples that could be scanned in our

265   AFM device, we mapped 4 pre-shear surfaces of a diorite sample as a proxy for gabbro. Figs.

266   4A-D display typical AFM surface maps that show only the areas above the mean height, with

267   areas below the mean height blacked out. This cutoff is based on the assumption that only

268   asperities above the mean height would interact with the other block. The distributions of the

269   local slopes (Fig. 4E, F) were determined for the areas above the average height in 26 AFM sites

270   (Appendix). The determined distributions reveal a few distinct features (Table 2):

271   (1) For pre-shear surfaces, the local slopes range from 0° to 75°. The frequency distribution of the

272   slopes indicates that 90% ± 4% are steeper than 6°, and that 54% ± 16% are steeper than 17°.

273   Namely, most of the asperities above the mean height are expected to fail according to

274   equation 4 (compare with Table 1);

275   (2) Sheared surfaces have a smaller portion of steep slopes than pre-shear surfaces, indicating the

276   elimination of asperities by wear of the steeper parts during shear (Figs. 4E, F).

277   These geometric features and the implied failure susceptibility agree with the model

278   conditions, and strongly support the validity of the central assumption that asperity failure

controls the stick-slips. While we focus here on unstable stick-slips, many quasi-static shear analyses documented the failure of isolated asperities or sets of asperities (Fig. 1) (Scholz and Engelder, 1976; Boneh et al., 2014; Tesei et al., 2017; Yamashita et al., 2018). We envision that the mechanical control of the asperity failure in those cases is also the local surface slope as analyzed and documented here.
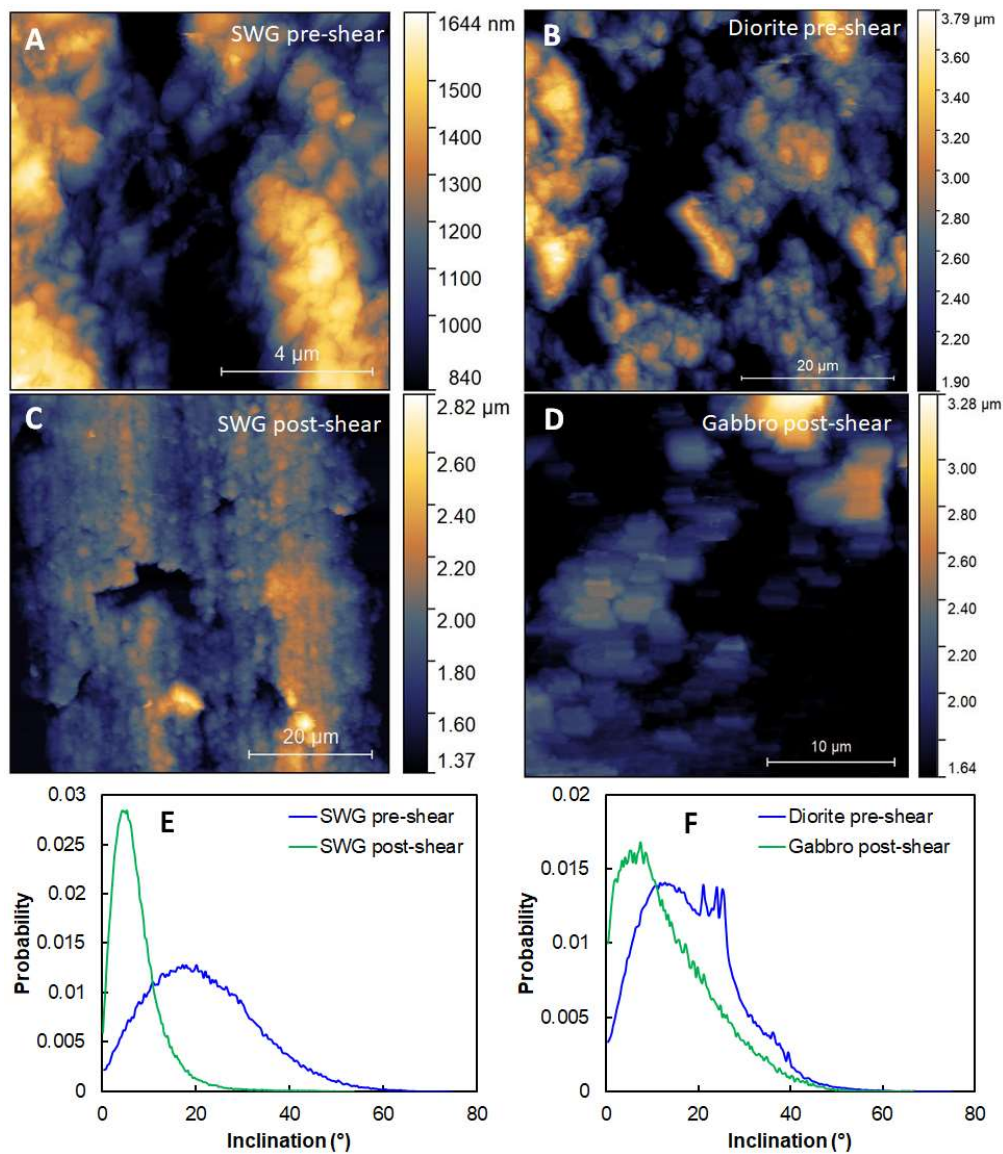
Figure 4. *Typical AFM topographic images of pre-shear and post-shear slip surfaces for granite, gabbro, and diorite samples (A-D) and their associated inclination probability distribution (E, F). A diorite pre-shear is used as a proxy to the pre-shear gabbro (see text).*

4.2 ASPERITY STRENGTH

In this section, we evaluate the asperity strength U_i as appeared in equation 1, and we employ a few strength terms. The 'yield-strength' and 'ultimate-strength' parameters (Fig. 5A, B) are commonly used in rock mechanics analysis (Lockner, 1995). The 'hardness' parameters (Tables 1, 2) was previously used to evaluate asperities' strength (Tabor, 1975; Dieterich and Kilgore, 1996; Boneh and Reches, 2018).Inherent strength' is also used in the analysis of internal friction. For example, Savage et al. (1996) found that faulting of intact granite samples is dominated by microcracks and bridges of intact rock between the micro-cracks. In their model, macroscopic failure occurred by frictional slip along the microcracks and shear failure of the intact bridges. Savage et al. (1996) showed through experimental observations that the strength of the intact bridges is the inherent strength, S_I, of the granite, and evaluated S_I ~1,000 MPa. They further realized that this value is in the right order of the ultimate strength of a perfect material after Hirth and Lothe (1968). We now show that the inherent strength is an effective parameter to evaluate the asperity strength, namely that $U_i \sim S_I$.

We first examine the structure and distribution of the asperities. The analyses of fault surface geometry reveal self-affine roughness from sub-micron scale in experiments (Chen et al., 2013), to tens of meter of active natural faults (e.g., Power et al., 1988; Sagy et al., 2007). Three characteristic features of these rough surfaces are relevant here. First, the elevated asperities (Fig. 4) are likely to contact and lock against the elevated asperities on the other fault block. The AFM maps show that ~25% of the pre-shear surfaces is susceptible to failure, and ~12% after shear (Fig. 4, Table 2). Second, the elevated asperities are isolated as observed in the fault surface maps (Fig. 4A, B), and views of smeared asperities on fault surfaces (Fig. 1A-C). Third, experimental observations confirmed that the touching asperities are separated by large regions of no contact under normal load (Fig. 1D). Due to their separation, the isolated asperities lock-and-fail independently, and as discussed above, the failure is facilitated by the local stress amplification and local slope (Table 2; Fig. 4) (Greenwood and Williamson, 1966; Whitehouse and Archard, 1970; Tabor, 1975; Byerlee, 1970, Dieterich and Kilgore, 1996). This occurrence of isolated, elevated asperities that are susceptible to failure is the central component of the present model (Fig. 2), and this failure is manifested in the macroscopic experimental stick-slips (e.g., Fig. 3).

14

318   The shear stress evolution in Fig. 5A indicates that during the sticking phase there is an elastic

319   stage, a yielding point of transfer to a creep stage, up to the peak stress, which is followed by the

320   slip phase. This evolution is practically the same as in typical rock-mechanics experiment (Fig.

321   5B) with a sequence of linear-elastic, yield point and strain-hardening to the ultimate strength

322   (e.g., Wawersik and Brace, 1971). Further, the macroscopic peak values of the shear-stress and

323   normal-stress during slip initiation display a linear Coulomb-Mohr relationship as shown in Fig.

324   5C for both SWG and RNG. These relationships are similar to the failure relationships of brittle

325   rocks, indicating that the stick-slip event is a solid asperity failure as hypothesized in the present

326   model (Fig. 2).

327   However, the magnitudes of the peak stresses of the stick-slips (Fig. 5C) are significantly

328   smaller than the corresponding stresses of rock failure, which are in the range of hundreds of

329   MPa, e.g, Fig. 5B (Lockner, 1995). This apparent contrast reflects the geometry of fault surface:

330   The real contact area, A_a, of the locked asperities is only a small fraction of the nominal area, A_o,

331   and therefore, the measured, <u>macroscopic</u> stresses are also small. Tabor (1981, Fig. 7) found that

332   on metal surfaces, which were prepared with an engineering finish, the real contact area is $A_a =$

333   σ_n / S_T where S_T is the plastic strength of the metal, and that cyclical normal loading may increase

334   the contact area to $A_a = (3\sim10)\cdot \sigma_n / S_T$. As discussed at the beginning of this section, Savage et

335   al. (1996) evaluated the inherent strength of granite as $S_I \sim 1,000$ MPa, and we infer that the

336   brittle S_I of Savage et al. (1996) is equivalent to the plastic S_T of Tabor (1981). By adopting this

337   equivalence, we find that the macroscopic shear-stress range of 4-10 MPa (Fig. 5C) corresponds

338   to local shear-stress of 400-1,000 MPa at the asperities for real contact area of $A_a \sim 0.01\cdot A_o$. This

339   contact area is in close agreement with the findings of Dieterich and Kilgore (1996) for quartz

340   and calcite under macroscopic normal stress of $\sigma_n = 30$ MPa (Fig. 1D).
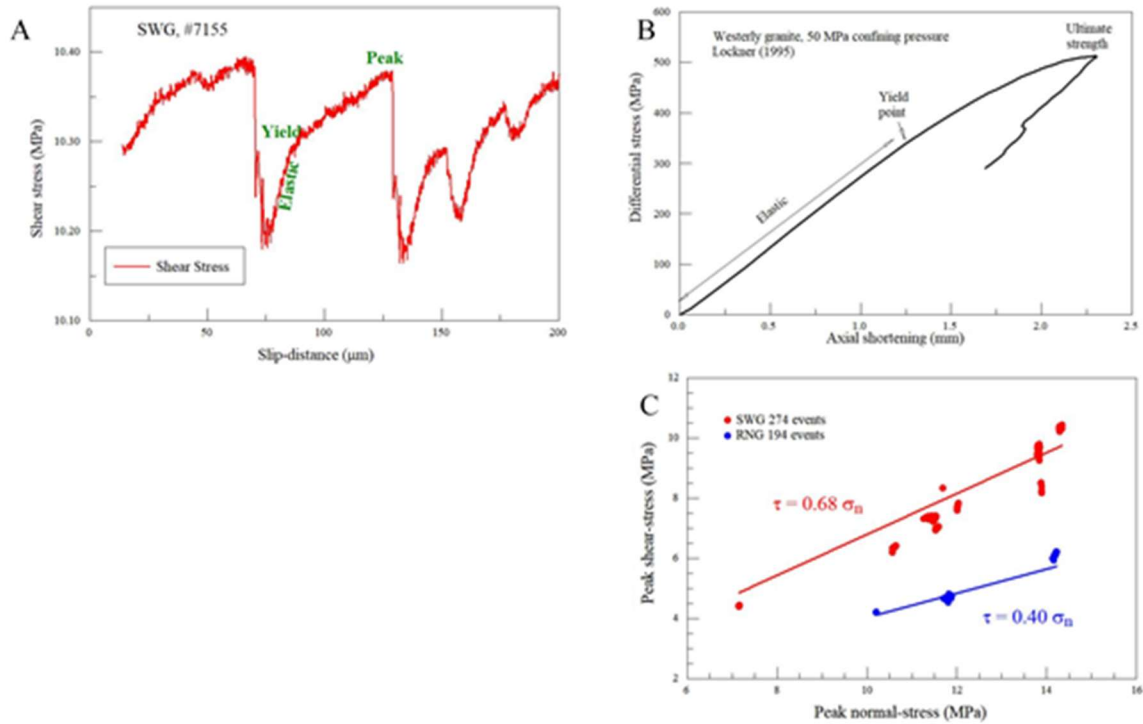
Figure 5. *Loading and failure in stick-slip and rock-mechanics experiments. A. Shear stress as a function of slip distance during four stick-slip events along SWG (experiment 7155, detail of Fig. 3B). B. Differential stress as function of axial shortening during failure experiment of Westerly granite under servo-control (after Lockner, 1995); note similarity of failure stage with the stick-slip event in A. C. Mohr diagram for peak stresses of the analyzed stick-slip experiments.*

We conclude that the asperities strength in the present experiments, U_i, is approximately equal to the inherent strength of the tested rocks, S_I. Further, these relationships explain the common observation that isolated asperities are pulverized into fine-grain powder even under small slip distance and low slip velocity (Fig. 1) (Byerlee, 1966; Boneh et al., 2014). The local pulverization indicates brittle fragmentation of the touching asperities as assumed in the model (Fig. 2).

4.3 SLIP-DISPLACEMENT AND STRESS-DROP

In our experimental system, we continuously monitored the global displacement D_m between the two fault blocks by using an Eddy current sensor with sub-micron resolution (Boneh et al., 2014) as shown in Figs. A1B, C. During stable slip, the total displacement on the fault equals the global displacement, but during a stick-slip event, the displacement on the fault surface also

16

358   includes a contribution of the elastic relaxation of the two rock blocks. The total displacement

359   during an event, D_i, is calculated by using the independently measured elastic stiffness of the

360   loading system, K, by

361    $$D_i = \frac{\Delta\tau_i}{K} + D_m \qquad (5)$$

362   where $\Delta\tau_i$ is the stress drop during the stick-slip event (equation 2). The linear relationships

363   between the stress-drop and the slip-displacements, for both measured D_m and calculated D_i, are

364   displayed in Fig. 6A.

365   In the present model (Fig. 2), the slip-displacement during an event is controlled by the

366   distance, D_i, between the lock-and-fail asperity #1, and the new locking asperity #2 (Fig. 2).

367   Thus, the distances between the asperities determine the slip-distances and as a consequence, the

368   distances also determine the stress-drops (equations 2, 5). We measure the distances between the

369   peaks of the high asperities in three of the AFM maps of the SWG (see Appendix for details). We

370   assume that the lock-and-fail mechanism operates between high asperities, and compare the

371   frequency distribution of the measured distances (blue curve in Fig. 6B) with the frequency

372   distribution of the slip-displacement during the SWG stick-slip event (red curve in Fig. 6B). The

373   distribution curves have similar shapes shifted by ~ 1 μm. This similarity between these two

374   independent measurements supports the model assumption that the slip-displacement is

375   controlled by the high, touching asperities.
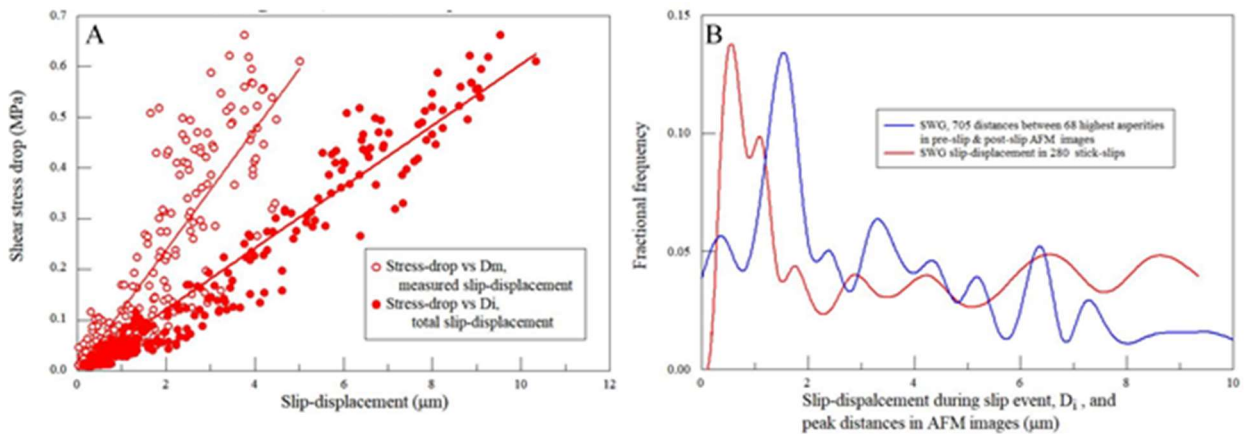
376

377   **Figure 6.** *Slip-displacements, stress-drops, and surface roughness in SWG experiments. A.*

378   *Measured stress-drop of 280 stick-slip events along the SWG fault as function of slip-*

379   *displacements, D_m and D_i (see text). B. Frequency distribution of 705 distances between high*

17

380   *asperities in Fig. A2A-C (blue curve), and frequency distribution of slip-displacements in 280*

381   *stick-slip events (red curve) (see Appendix).*

382   **5. DISCUSSION**

383   5.1 STICK-SLIPS AS A FRACTURE PROCESS

384   The present analysis considers stick-slips along bare, flat rock faults. The real contact area of

385   such a fault is at isolated, touching asperities that cover 0.1-2.0% of the nominal area (Fig. 2, 4)

386   (Dieterich and Kilgore, 1996). Only the touching asperities can resist slip along the fault while

387   the non-touching spaces between the isolated asperities do not contribute to the slip resistance.

388   Inspection of the surfaces of bare, flat rock faults has systematically revealed elongated striations

389   of smeared powder of fragmented, isolated asperities (Fig. 1) (Scholz and Engelder, 1976; Boneh

390   et al., 2014; Yamashita et al., 2018; Tesei et al., 2017; Boneh and Reches, 2018). Therefore, the

391   central concept here is that slip along a brittle experimental fault initiates when touching

392   asperities fail by fracturing. Brace and Byerlee (1966) explored "Stick-slip as a mechanism for

393   earthquakes" by testing Westerly granite samples which were either intact or with an initial saw-

394   cut. Their experiments revealed jerky, irregular stick-slips (Fig. 6B) under high confining

395   pressure (up to 650 MPa) while generating similar stick-slips for both intact samples and saw-cut

396   samples. This similarity suggests that 'frictional slip' along a saw-cut sample is essentially

397   controlled by fracturing.

398   Brittle fracturing of isolated, contacting asperities is considered here as the controlling process

399   of stick-slips, yet, the contact area evolution could not be monitored in the opaque rock samples.

400   This limitation can be removed in shear experiments with fault composed of transparent brittle

401   polymer (PMMA) (Rubinstein et al., 2011; Svetlizky and Fineberg, 2014). Svetlizky and

402   Fineberg (2014) measured in high-resolution stick-slip ruptures along a planar PMMA interface

403   and observed that the strain fields around the rupture front perfectly fits the classical theory of a

404   rapid brittle fracture (Freund, 1990). They also found that the linear weakening slip-displacement

405   at the rupture front is about 1.4 μm, which is compatible with interface roughness of ~3 μm rms.

406   This analysis was furthered by Bayart et al., (2016) who focused on rupture arrest and the slip-

407   distance associated with experimental stick-slips. They stated that the "results provide clear

408   evidence that frictional rupture is really a fracture process that can be quantitatively described by

409 fracture mechanics. The concepts presented here suggest a completely different paradigm for

410 understanding friction from that of the classical picture, which is based on the balance of local

411 forces (stresses)."

412   While the PMMA experiments indicate that dynamic rupture is a fracture phenomenon, and

413 the present rock experiments are consistent with brittle asperity fracturing, stick-slip behavior is

414 almost universally analyzed in terms of static and dynamic friction coefficients (e.g., Karner and

415 Marone, 2000). The friction coefficient is an easily measured parameter, but it carries no direct

416 physical mechanism. We thus argue that while the usage of friction coefficient(s) is convenient,

417 the mechanics of fracturing provides a clearer insight to stick-slip processes.

418 5.2 APPLICATION TO GRANULAR LAYERS AND GOUGE-FILLED FAULTS

419   In the present analysis, we consider an experimental fault composed of a planar, rough, bare

420 rock surface (Fig. 2), along which the local stress amplification is controlled by touching

421 asperities. We infer, however, that the derived mechanics may be valid to other configurations in

422 which local failure leads to macroscopic stick-slips, for example, along experimental faults with a

423 gouge layer. We outline below two failure mechanisms within a gouge layer that are compatible

424 with the present stick-slip mechanics.

425   The first failure mechanism is based on the 'effective asperity' concept developed by Boneh

426 and Reches (2018) in their analysis of brittle wear along fault with a gouge layer (Fig. 7A). In

427 this case, the fracturing which occurs at the contact between the gouge layer and the fault blocks

428 (Lyakhovsky et al., 2014) modifies the contact roughness and forms new large particles, defined

429 as 'effective asperities' (Boneh and Reches, 2018). While these new asperities differ in shape and

430 size from the originals (Fig. 7A), they also amplify the local stresses because they do not deform

431 as easily as the surrounding gouge. The amplified local stresses are expected to lead to intense

432 local fracturing, including sub-surface fracturing of the rock blocks (Fig. 7A) (Lyakhovsky et al.,

433 2014). If this local fracturing occurs unstably, it would generate macroscopic stick-slips in a

434 similar style to the present mechanism.

435   Another mechanism that can generate stick-slips is the unstable failure of highly stressed

436 force-chains within a granular layer. It is well documented, both experimentally and numerically,

437 that shear loading of a granular layer is supported mostly, if not completely, by a network of

438   isolated force-chains (Fig. 7B) (e.g. Majmudar and Behringer, 2005). With continuous shear, the

439   fault with the granular layer exhibits macroscopic stick-slips that most analysis attribute to

440   unstable collapse of the force-chains (e.g. Scuderi et al., 2014), while usually the experiments are

441   designed to limit the possible fracturing of the grains. However, we envision that the highly

442   stressed grains are very susceptible to brittle fracturing and thus propose that stick-slips along

443   faults with a granular layer are controlled by local, brittle fracturing within the isolated stress-

444   chains. We further suggest that the mechanics of the associated stick-slip would fit the framework

445   of the present model.
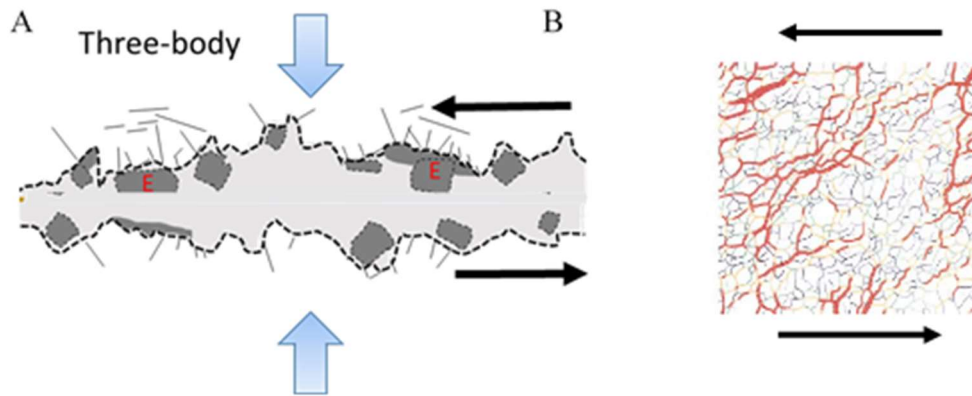
446

447   **Figure 7.** *A. A fault with a gouge layer (light grey) that includes large, coarse grains (dark grey)*

448   *which act like effective asperities with increased local stress (after Boneh and Reches, 2018). B.*

449   *Simulated stress field within a granular layer subjected to shear; the grains contacts are not*

450   *shown; line thickness is scaled to the largest stress (after Aharonov and Sparks, 2002).*

451   **6. CONCLUSIONS**

452   The present analysis of brittle fracturing of isolated asperities provides significant insight into

453   a few distinct features of experimental stick-slip behavior.

454   **A.** We evaluate the strength of fault asperities as 400-1,000 MPa based on the experimental

455   shear and normal stresses and the contact area of touching asperities (Fig. 5). This strength is

456   in the range of the inherent shear strength of intact, perfect rock as shown by Savage et al.

457   (1996). The inherent strength reflects the local stress-state of the failing asperity.

458   **B.** In the present analysis, we applied the material hardness, H, as an effective variable in

459   characterization of fracture tendency of fault asperities (Tables 1, 2). Hardness is measured at

460 small scales, which are relevant to the asperities' size, and it integrates multiple failure

461 properties.

462 **C.** The analysis explains why fragmentation and wear can be reduced by surface smoothing that

463 reduces the asperities inclination, θ, and increases the real contact area, A_a; both these

464 geometric features reduce local stresses and fracture tendency. Further, as dissipation of

465 fracture energy is a contribution component to frictional resistance (Boneh et al., 2014),

466 smoother rock surfaces, with less fracturing, would display lower friction coefficients (Chen

467 et al., 2013).

468 **D.** According to the present model, the stress-drop during stick-slip is determined by the

469 distances between locking asperities, and controlled by the system stiffness (Figs. 2, 6). This

470 inference could have significant implications to fault behavior. The distances between

471 potentially locking asperities depend on fault roughness. As these distances are larger on a

472 smooth fault, it is anticipated that a smooth fault will generate more intense (stress-drop and

473 slip-distance) stick-slips than a rough fault in the same system (e.g., Ohnaka, 1973). We thus

474 speculate that quantification of fault roughness in terms of both power spectral density (Fig.

475 6C) and local slope (Fig. 4) could predict the intensity of the stick-slips.

483   Table 1. Rock mechanical properties and calculated critical asperity slope for brittle failure.

Rock/mineral/ material	Modulus E, GPa	Hardness H, GPa	E/H	Critical angle
Granite	38-75[a]	8.8-11.4[d]	3-8	> 7° - 17°
Gabbro	50-115[b]	12-15[d]	3-9	> 6° - 19°
Quartz		14.5[c]		
Orthoclase		9.1[c]		
Calcite		2.2[c]		
Pure metal (annealed)			200-400[e]	> 0.5°
Ceramic			20-30[e]	5°
Cross-linked plastics			3-5[e]	> 20°

484   a- Katz et al. (2001)

485   b- Keshavarz et al. (2010)

486   c- Broz et al. (2006)

487   d- Estimated from Broz et al. (2006)

488   e- Critical strength/slope for plastic deformation, Tabor (2006)

489

490

491

492

493

494 Table 2. Summary of AFM surface characterization (Fig. 3 and Appendix)

|		Slopes (for upper half)	
		fraction > 6°	fraction > 17°
Granite	pre-shear	90% ± 4%	54% ± 16%
	post-shear	74% ± 12%	25% ± 15%
Diorite	pre-shear	87% ± 1%	48% ± 6%
Gabbro	post-shear	79% ± 3%	35% ± 6%

495

496 **APPENDIX**

497 EXPERIMENTAL SET-UP

498   The high-velocity, rotary shear apparatus (ROGA) (Reches and Lockner, 2010) was modified
499 to include an integrated low-velocity capability driven by a stepper motor for slip-velocities of
500 0.25 μm/s to 1 mm/s (item 4 in Fig. S1A). The experimental fault has a ring-shaped contact
501 between a lower solid rock blocks (10.2 cm diameter and 5 cm height) and an upper block with
502 raised ring (Fig. S1B). The gabbro fault has inner diameter of 62 mm and outer diameter of ~84
503 mm, while the SWG fault has inner diameter of 61.4 mm and outer diameter of 84.5 mm. Bare
504 rock surfaces with #600 grit roughening were used for the present tests. Rotation is applied to the
505 lower block by the stepper motor and the upper block is stationary. The normal and shear stresses
506 were monitored by load cells, the displacement between the two fault blocks was monitored with
507 an eddy current sensor, and the velocity and displacement were controlled with a stepper motor
508 system. The experimental data were continuously recorded with a dedicated Labview program at
509 sampling rate of 3k-5k Hz.

510 EXPERIMENTAL PROCEDURE

511   The typical procedure for the shear experiments includes the following steps. First, load the
512 sample, attach the displacement sensor. Second, set and apply the desired normal stress on the
513 fault. Third, use the stepper motor system to load the fault at desired velocity and duration.
514 Typical driving speed is 1-10 μm/s, and typical loading duration is 10-20 s. The normal stress
515 was kept constant during the shear and can be adjusted in between shear. At lower normal
516 stresses of <10 MPa, both SWG and RNG faults slide stably without any stick-slips. At higher
517 normal stresses, stick-slips start to occur. The experimental conditions and results summery are
518 listed in Table A1.

519
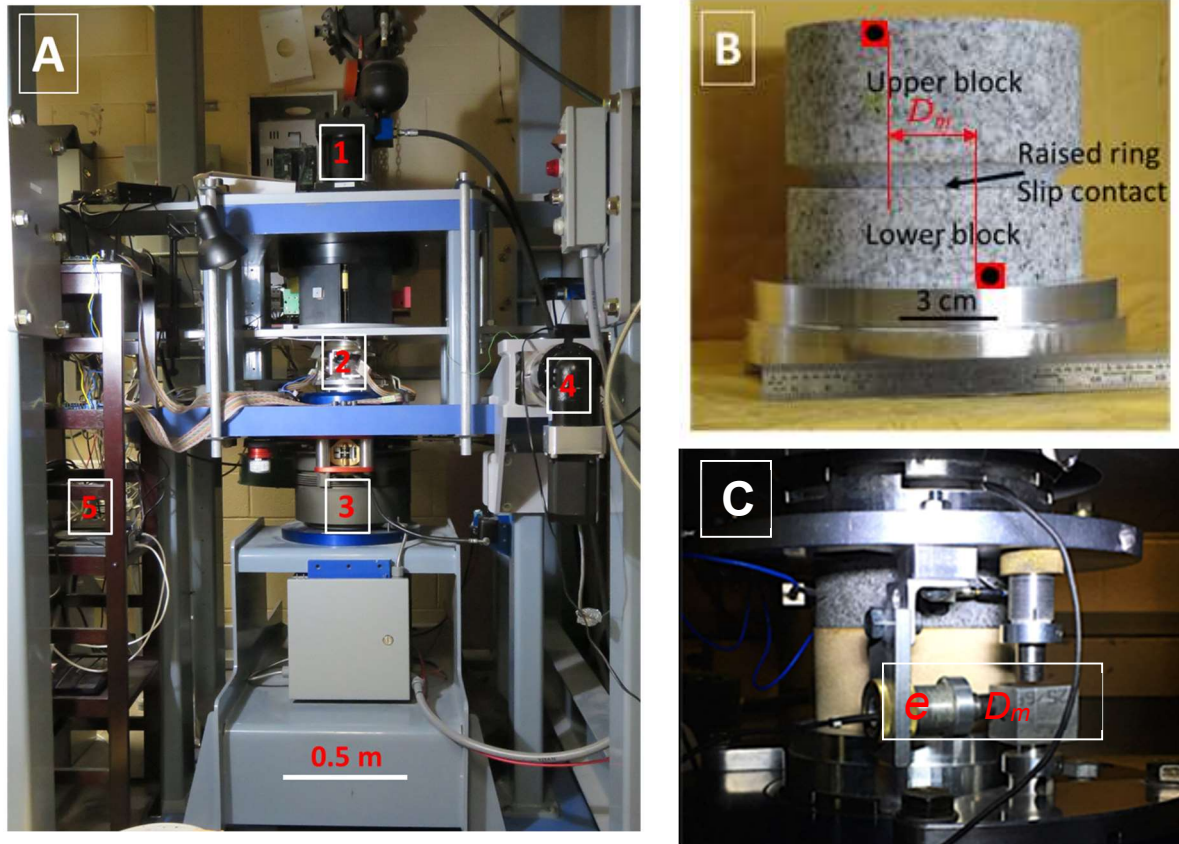
520

521 **Figure A1**. *The ROAG apparatus (Reches and Lockner, 2010). A. The apparatus with marked*
522 *load cell (1), sample loading site (2), electric-magnetic clutch (3), step motor arm for low*
523 *velocity tests (4), and high-frequency strain-gauge sampling hardware for rupture propagation*
524 *monitoring (5). B. The fault rock samples of SWG with schematic presentation of the measuring*
525 *slip, D_m, between top and bottom of the fault blocks. C. Photo of a bi-material fault with a*
526 *horizontal eddy-current sensor (e) and location of D_m.*

527

528 AFM MAPPING OF FAULT SURFACES

529 We used AFM (atomic force microscope) from Asylum Research to map topography of both

530 the pre-shear rock surface and the post-shear fault surface. The topologic images were acquired

531 under the AC mode (tapping) in ambient room conditions, with typical scan area of a few μm up

532 to 60 μm across with resolution up to 1024 by 1024 pixels. We mapped 6 polished pre-shear

25

533   surfaces and 13 post-shear surfaces from SWG, 4 post-shear surfaces from gabbro, and 4 pre-

534   shear surfaces from a diorite as an approximate to gabbro (no available pre-shear gabbro surface

535   for AFM). Typical maps are displayed in Fig. 3. The two-dimensional height distribution and

536   surface inclination distribution (Fig. 4E, F) are extracted from the AFM topographic map using

537   the Gwyddion software available online (http://gwyddion.net).

538   We measure the distances between the peaks of the highest asperities in three of the AFM

539   maps of SWG. The peaks of the highest asperities were first digitized (white points in Fig. A2)

540   and then the distances were calculated. In the pre-shear maps (Fig. A2A, B) the distances were

541   calculated between all marked highest asperities (note scales of maps). In the post-slip map (Fig.

542   A2C), which displays clear slip striations, the asperity distances were calculated between

543   neighboring marked high asperities; we assume that the lock-and-fail mechanism operates only

544   parallel to the slip direction. Note that the used images display the upper 50% of the surface

545   elevation and the lower 50% is colored black.

546
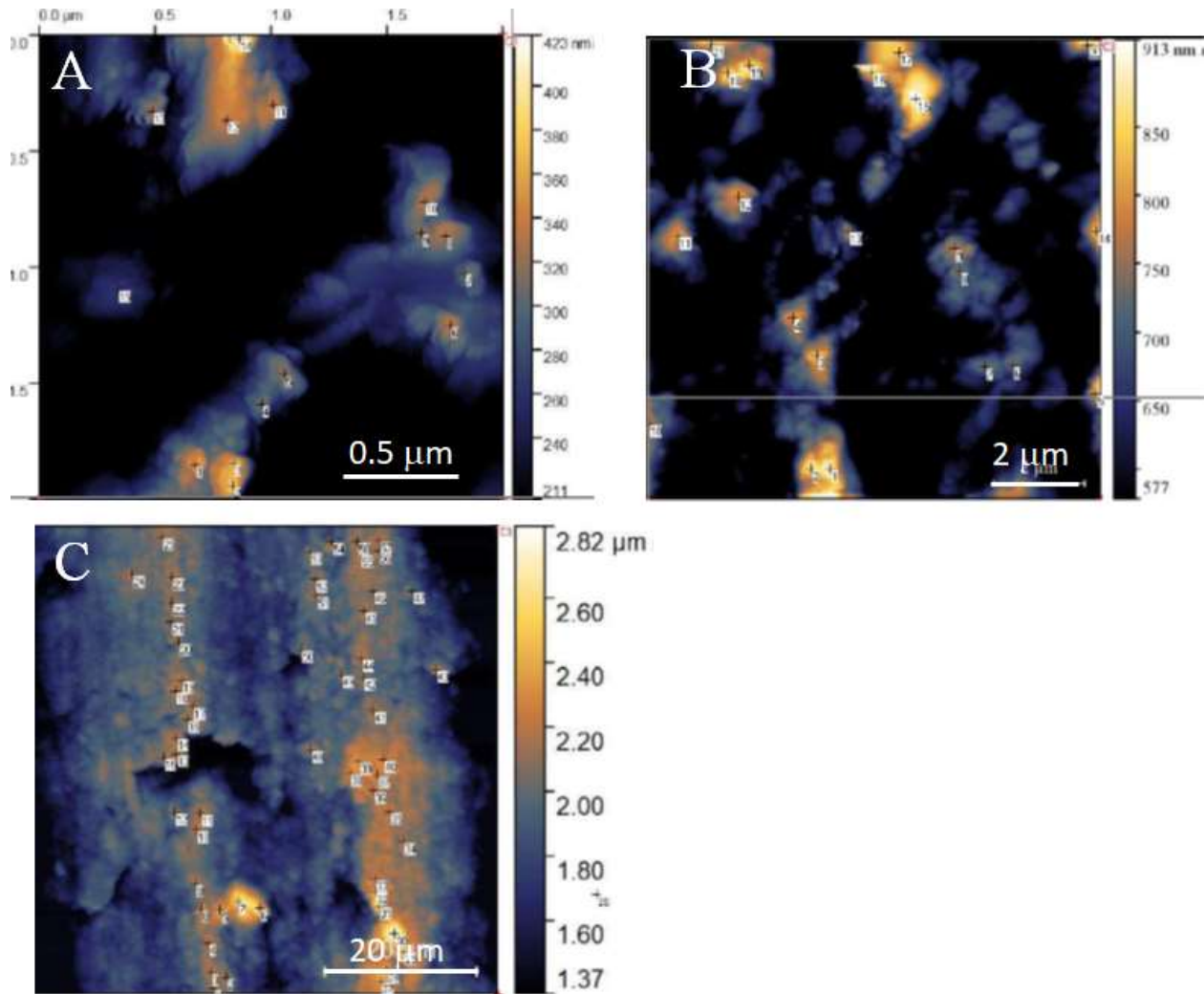
547 **Figure A2.** *Surface topography of SWG fault surfaces as mapped by AFM. The images display*

548 *the upper 50% of the surface elevation and the lower 50% is colored black. The digitized peaks*

549 *of the high asperities are marked by small white squares. A, B. Pre-slip AFM images; note*

550 *scales. C. Post-slip AFM image. A total of 705 distances were calculated in A-C (see text).*

551

Table A1. Experimental conditions and summary of main results

	Run #	Normal stress	Applied velocity	# events	Event Ranges			
					stress drop	displacement	rise time	max velocity
		MPa	μm/s		MPa	μm	ms	μm/s
Sierra White granite	7152	14.3	308	10	0.024-0.04	0.73-1.80	1-1.6	726-1,040
	7154	14.3	185	7	0.065-0.081	1.26-2.19	1-1.2	875-1,172
	7155	14.3	617	21	0.043-0.158	1.72-5.02	1.2-1.6	1,057-3,451
	7160	13.9	617	41	0.038-0.512	1.41-9.16	0.6-1.5	1,321-12,177
	7161	13.8	62	20	0.069-0.387	1.21-6.68	0.75-1	1,770-7,423
	7162	13.8	62	14	0.04-0.619	1.04-10.86	0.75-1.25	1,057-13,076
	7163	13.8	185	44	0.033-0.663	0.83-11.92	0.75-1.5	1,162-14,159
	7164	13.7	19	8	0.06-0.170	1.31-3.14	0.75-0.88	1,400-4,755
	7165	13.8	19	3	0.034-0.042	0.65-0.83	0.75	1,057-1,506
	7166	13.8	185	13	0.046-0.314	1.07-6.09	0.75-1	1,426-7,053
	7416	10.6	308	5	0.015-0.022	0.31-0.43	0.6-0.8	188-3,944
	7417	10.5	308	12	0.01-0.020	0.09-0.67	0.6-1.2	562-3,569
	7419	11.5	308	13	0.009-0.045	0.22-1.18	0.4-0.8	376-3,193
	7430	11.3	62	3	0.013-0.028	0.22-0.41	0.6-0.8	564-7,50
	7431	11.3	617	2	0.025-0.028	0.22-0.36	0.6	376
	7432	11.3	617	7	0.012-0.058	0.33-1.03	0.6-0.8	374-,1691
	7433	11.4	617	8	0.017-0.055	0.17-1.09	0.4-1.2	188-1,127
	7434	11.4	617	15	0.012-0.052	0.23-0.72	0.4-0.8	188-1,435
	7435	11.5	617	7	0.016-0.026	0.24-0.52	0.6-1.2	188-1,435
	7436	11.5	617	19	0.015-0.116	0.24-1.05	0.4-1	188-1,691
	7460	11.6	617	2	0.013-0.017	0.63-0.66	0.6	940-1,128
	7464	12.0	617	7	0.029-0.063	0.82-1.16	0.6-0.8	1503-2,067
Raven Noir gabbro	7298	11.8	9.54	103	0.053-0.114	4.25-5.75	147-270	28-49
	7299	11.7	9.54	10	0.068-0.081	4.02-5.15	192-206	32-38
	7300	11.8	1.03	16	0.268-0.458	9.65-15.91	207-360	129-235
	7301	11.8	0.26	10	0.345-0.477	12.17-17.58	110-340	184-257
	7302	11.8	0.26	3	0.155-0.196	3.59-4.82	286-350	30-46
	7304	11.8	0.26	5	0.357-0.598	7.38-12.23	244-496	97-162
	7305	11.8	0.52	6	0.312-0.411	6.44-8.41	218-412	80-116
	7306	11.8	1.03	7	0.254-0.421	5.35-8.46	233-380	61-128
	7307	11.9	2.06	7	0.186-0.391	3.82-8.13	133-284	42-113
	7308	11.9	3.87	9	0.122-0.416	3.25-8.66	101-243	29-128
	7316	14.2	3.87	9	0.125-0.473	4.66-12.9	103-268	29-200
	7318	14.2	1.03	4	0.328-0.332	7.70-7.80	287-339	94-100
	7319	14.2	0.52	7	0.381-0.479	8.98-10.74	300-446	115-153
	7320	14.2	0.26	6	0.435-0.506	10.34-11.95	555-755	151-185
	7321	10.2	0.26	7	0.307-0.372	8.91-10.67	505-780	125-169

<div align="center">**REFERENCES**</div>

554

555 Aharonov, E., Scholz, C. H., 2018. A physics-based rock friction constitutive law: Steady state
556   friction. Journal of Geophysical Research: Solid Earth, 123, 1591–1614. doi:10.1002/
557   2016JB013829.

558 Aharonov, E., Sparks, D., 2002. Shear profiles and localization in simulations of granular
559   materials. Physical Review E, 65(5), 051302. doi:10.1103/PhysRevE.65.051302.

560 Bayart, E., Svetlizky, I., Fineberg, J., 2016. Fracture mechanics determine the lengths of interface
561   ruptures that mediate frictional motion. Nature Physics, 12, 166-170. doi:
562   10.1038/nphys3539.

563 Boneh, Y., Chang, J. C., Lockner, D. A., Reches, Z., 2014. Evolution of wear and friction along
564   experimental faults. Pure and Applied Geophysics, 171, 3125-3141. doi: 10.1007/s00024-
565   014-0801-3.

566 Boneh, Y., Reches, Z., 2018. Geotriboloty – Friction, wear, and lubrication of faults.
567   Tectonophysics, 733, 171-181. doi:10.1016/j.tecto.2017.11.022.

568 Brace, W. F., Byerlee J. D., 1966. Stick-slip as a mechanism for earthquakes. Science, 153, 990-
569   992. doi:10.1126/science.153.3739.990.

570 Broz, M. E., Cook, R. F., Whitney, D. L., 2006. Microhardness, toughness, and modulus of Mohs
571   scale minerals. American Mineralogist, 91(1), 135-142. doi:10.2138/am.2006.1844.

572 Byerlee, J. D., 1967. Frictional characteristics of granite under high confining pressure. Journal of
573   Geophysical Research, 72, 3639-3648. doi:10.1029/JZ072i014p03639.

574 Byerlee, J. D., 1970. The mechanics of stick-slip. Tectonophysics, 9, 475-486. doi:10.1016/0040-
575   1951(70)90059-4.

576 Chen, X., Madden, A. S., Bickmore, B. R., Reches, Z., 2013. Dynamic weakening by nanoscale
577   smoothing during high-velocity fault slip. Geology, 41, 739-742. doi:10.1130/G34169.1.

578 Das, S., Kostrov, B. V., 1986. Fracture of a single asperity on a finite fault: A model for weak
579   earthquakes?. Earthquake Source Mechanics, 37, 91-96.

580 Di Toro, G., Han, R., Hirose, T., De Paola, N., Nielsen, S., Mizoguchi, K., Shimamoto, T., 2011.
581   Fault lubrication during earthquakes. Nature, 471, 494–498. doi:10.1038/nature09838.

582   Dieterich, J. H., 1978. Time-dependent friction and the mechanics of stick-slip. Pure and Applied
583   Geophysics, 116, 790-806. doi:10.1007/978-3-0348-7182-2_15.

584   Dieterich, J. H., Kilgore, B. D., 1996. Imaging surface contacts: power law contact distributions
585   and contact stresses in quartz, calcite, glass, and acrylic plastic. Tectonophysics, 256, 219-
586   239. doi:10.1016/0040-1951(95)00165-4.

587   Engelder, J. T., Scholz, C. H., 1976. The role of asperity indentation and ploughing in rock
588   friction - II: Influence of relative hardness and normal load. International Journal of Rock
589   Mechanics and Mining Sciences & Geomechanics Abstracts, 13, 155-163. doi:10.1016/0148-
590   9062(76)90820-2.

591   Freund, L. B. Dynamic Fracture Mechanics, Cambridge, 1990.

592   Greenwood, J. A., Williamson, J. B. P., 1966. Contact of nominally flat surfaces. Proceedings of
593   the Royal Society A. 295, 300-319. doi:10.1098/rspa.1966.0242.

594   Hirth, J.P., and Lothe, J., 1968. Theory of Dislocations, 780 pp., McGraw-Hill, New York.

595   Ikari, M. J., Carpenter, B. M., Marone, C., 2016. A microphysical interpretation of rate- and
596   state- dependent friction for fault gouge, Geochemistry, Geophysics, Geosystems, 17, 1660–
597   1677. doi:10.1002/2016GC006286.

598   Jaeger, J. G., Cook, N. G. W., 1969. Fundamentals of rock mechanics. Methuen, London.

599   Karner, S., Marone, C., 2000. Effects of loading rate and normal stress on stress drop and stick-
600   slip recurrence interval. in Rundle, J., Turcotte, D., & Klein, W. eds. Geocomplexity and the
601   physics of Earthquakes. AGU Geophysical Monograph 120, 187-198.
602   doi:10.1029/GM120p0187.

603   Katz, O., Reches, Z., Roegiers, J. C., 2000. Evaluation of mechanical rock properties using a
604   Schmidt Hammer. International Journal of rock mechanics and mining sciences, 37(4), 723-
605   728. doi:10.1016/S1365-1609(00)00004-6.

606   Keshavarz, M., Pellet, F. L., Loret, B., 2010. Damage and changes in mechanical properties of a
607   gabbro thermally loaded up to 1,000 °C. Pure and Applied Geophysics, 167, 1511-1523.
608   doi:10.1007/s00024-010-0130-0.

609   Koizumi, Y., Otsuki, K., Takeuchi, A., Nagahama, H., 2004. Frictional melting can terminate

610   seismic slips: Experimental results of stick-slips. Geophysical Research Letters, 31, L21605.

611   doi:10.1029/2004GL020642.

612   Leeman, J. R., Marone, C., Saffer, D. M., 2018. Frictional mechanics of slow earthquakes.

613   Journal of Geophysical Research: Solid Earth, 123, 7931–7949. doi:10.1029/2018JB015768.

614   Lockner, D. A., 1995. Rock failure, in Ahrens, T. J. ed. Rock physics & phase relations: a

615   handbook of physical constants, Volume 3. 127-147. doi: 10.1029/RF003p0127.

616   Lyakhovsky, V., Sagy, A., Boneh, Y., Reches, Z., 2014. Fault wear by damage evolution during

617   steady-state slip. Pure and Applied Geophysics, 171(11), 3143-3157. doi:10.1007/s00024-

618   014-0787-x.

619   Majmudar, T.S., Behringer, R.P., 2005. Contact force measurements and stress-induced

620   anisotropy in granular materials. *Nature*, *435*, 1079. doi:10.1038/nature03805.

621   McLaskey, G. C., Glaser, S.D., 2011. Micromechanics of asperity rupture during laboratory stick

622   slip experiments. Geophysical Research Letters, 38.12.

623   Niemeijer, A., Di Toro, G., Nielsen, S., Di Felice, F., 2011. Frictional melting of gabbro under

624   extreme experimental conditions of normal stress, acceleration, and sliding velocity. Journal

625   of Geophysical Research,116, B07404. doi:10.1029/2010JB008181.

626   Ohnaka, M. 1973. A physical understanding of the earthquake source mechanism. Journal of

627   Physics of the Earth, 21, 39-59. doi: 10.4294/jpe1952.21.39.

628   Ohnaka, M., Kuwahara, Y., Yamamoto, K., 1987. Constitutive relations between dynamic

629   physical parameters near a tip of the propagating slip zone during stick-slip shear failure.

630   Tectonophysics, 144, 109-125. doi:10.1016/0040-1951(87)90011-4.

631   Power, W. L., Tullis, T. E., Weeks, J. D., 1988. Roughness and wear during brittle faulting.

632   Journal of Geophysical Research: Solid Earth, 93, 15268-15278. doi:

633   10.1029/JB093iB12p15268.

634   Rastei, M. V., Heinrich, B., Callani, J. L., 2013. Puckering stick-slip friction induced by a sliding

635   nanoscale contact. Physical Review Letters, 111, 084301.

636   doi:10.1103/PhysRevLett.111.084301.

637   Reches, Z., Lockner, D. A., 2010. Fault weakening and earthquake instability by powder
638   lubrication. Nature,467, 452–455. doi:10.1038/nature09348.

639   Rubinstein, S. M., Barel, I., Reches, Z., Braun, O. M., Urbakh, M., Fineberg, J., 2011. Slip
640   sequences in laboratory experiments resulting from inhomogeneous shear as analogs of
641   earthquakes associated with a fault edge. Pure and Applied Geophysics, 168, 2151-2166. doi:
642   10.1007/s00024-010-0239-1.

643   Sagy, A., Brodsky, E. E., Axen, G. J., 2007. Evolution of fault-sirface roughness with slip.
644   Geology, 35, 283-286. doi: 10.1130/G23235A.1.

645   Savage, J. C., Byerlee, J. D., & Lockner, D. A., 1996. Is internal friction friction?. Geophysical
646   research letters, 23(5), 487-490.

647   Scholz, C. H., 1992. Paradigms or small change in earthquake mechanics. International
648   Geophysics, 51, 505-517. doi:10.1016/S0074-6142(08)62836-3.

649   Scholz, C. H., 1998. Earthquakes and friction laws. Nature, 391, 37-42. doi:10.1038/34097.

650   Scholz, C. H., Engelder, J. T., 1976. The role of asperity indentation and ploughing in rock
651   friction - I: Asperity creep and stick-slip. International Journal of Rock Mechanics and
652   Mining Sciences & Geomechanics Abstracts, 13, 149-154. doi:10.1016/0148-9062(76)90819-
653   6.

654   Scuderi, M. M., Carpenter, B. M., Marone, C., 2014. Physicochemical processes of frictional
655   healing: Effects of water on stick-slip stress drop and friction of granular fault gouge. Journal
656   of Geophysical Research: Solid Earth, 119, 4090-4105. doi:10.1002/2013JB010641.

657   Svetlizky, I., Fineberg, J., 2014. Classical shear cracks drive the onset of dry frictional motion.
658   Nature, 509, 205-208. doi:10.1038/nature13202.

659   Tabor, D., 1975. Interaction between surfaces: Adhesion and friction. in Blakely, J. M. eds.
660   Surface physics of materials, Ch. 10. Academic Press, New York, San Francisco, London.

661   Tabor, D., 1981. Friction – The present state of our understanding. Journal of Lubrication
662   Technology, 103, 169-179. doi:10.1115/1.3251622.

663   Tabor, D., 2006. Friction, lubrication, and wear, in Rothbart, H. A., Brown, T. H., eds.
664   Mechanical Design Handbook, Second Edition: Measurement, Analysis and Control of
665   Dynamic Systems, 7.1-7.25.

666 Tesei, T., Carpenter, B. M., Giorgetti, C., Scuderi, M. M., Sagy, A., Scarlato, P., Collettini, C.,

667   2017. Friction and scale-dependent deformation processes of large experimental carbonate

668   faults. Journal of Structural Geology, 100, 12-23. doi:10.1016/j.jsg.2017.05.008.

669 Wawersik, W. R., Brace W. F., 1971. Post-failure behavior of a granite and diabase, Rock

670   Mechanics, 3, 61– 85. doi: 10.1007/BF01239627.

671 Whitehouse, D. J., Archard, J. F., 1970. The properties of random surfaces of significance in their

672   contact. Proceedings of the Royal Society A, 316, 97-121. doi:10.1098/rspa.1970.0068.

673 Yamashita, F., Fukuyama, E., Xu, S., Mizoguchi, K., Kawakata, H., Takizawa, S., 2018. Rupture

674   preparation process controlled by surface roughness on meter-scale laboratory fault.

675   Tectonophysics, 733, 193-208. doi:10.1016/j.tecto.2018.01.034.

676